The effect of function-based and voxel-based tropospheric tomography techniques on the GNSS positioning accuracy

Saeid Haji-Aghajany[1, 2], Yazdan Amerian[1], Sandra Verhagen[2], Witold Rohm[3], Harald Schuh[4, 5]

[1]Faculty of Geodesy and Geomatics Engineering, K. N. Toosi University of Technology, Tehran, Iran

[2]Faculty of Civil Engineering and Geosciences, Delft University of Technology, Stevinweg 1, 2628 CN Delft, The Netherlands

[3]Institute of Geodesy and Geoinformatics Wroclaw University of Environmental and Life Sciences, Grunwaldzka 53, 50-357 Wroclaw, Poland

[4]GFZ German Research Centre for Geosciences, 14473, Potsdam, Germany

[5]Chair of Satellite Geodesy, Technische Universität Berlin, 10623 Berlin, Germany

Abstract

Tropospheric wet delay, the main source of which is water vapor, is one of the major factor affecting the accuracy of positioning techniques using microwave. Tropospheric tomography is a powerful method to reconstruct the water vapor content in four-dimensional (4D) space. This paper studies the effect of using function-based and voxel-based tropospheric tomography methods on the positioning accuracy. This examination is performed on the static and kinematic positioning modes using Global Navigation Satellite Systems (GNSS) stations under different weather conditions. After validating the results of tomography methods using radiosonde observations, the tomography-based positioning solutions, including function-based and voxel-based approaches, are compared with the positions obtained using tropospheric models. The results of two GPS stations show that the accuracy increases when applying tomography approaches. The function-based tomography is able to increase the accuracy of the up component of the static and kinematic modes by about 0.42 and 0.79 cm, respectively, compared to the voxel-based method. In addition, the use of the function-based tropospheric tomography can decrease the convergence time of the kinematic Precise Point Positioning (PPP) solution.

Keywords: GNSS, Precise point positioning, Tropospheric tomography, Function-based, Voxel-based

1. Introduction

Atmospheric effects, e.g., ionospheric effect and tropospheric effect, are the main error sources in PPP technique. The tropospheric delay is usually considered as an unknown parameter together with other factors

such as phase ambiguity and receiver coordinates (Hadas et al. 2013). Based on physical specifications, the zenith tropospheric delay (ZTD) can be divided into zenith hydrostatic delay (ZHD) and zenith wet delay (ZWD). ZHD is caused by the dry gas content in the troposphere layer. It can be accurately computed using empirical models (Saastamoinen 1973). ZWD is caused by water vapor in the troposphere layer and is complicated to get reconstructed due to the high spatiotemporal variations of this parameter. Precise tropospheric corrections can help to mitigate the tropospheric effect in GNSS signal processing, to reduce the number of unknowns and to accelerate the convergence time (Hadas et al. 2013). The tropospheric effect is closely correlated with the vertical component of positioning. It is necessary to have a high-precision spatiotemporal distribution of water vapor in order to increase the accuracy of positioning.

Many researchers proposed high-precision tropospheric corrections from GNSS reference networks for positioning techniques: interpolating tropospheric corrections from nearby GNSS stations (Li et al. 2011), using real-time correction from GNSS processing (Hadas et al. 2013), applying corrections from regional GNSS network (Shi et al. 2014), considering the tropospheric delay derived from a GNSS-based global troposphere model as virtual observations (Yao et al. 2014), presenting an inverse scale height model to produce real-time tropospheric delay (Lou et al. 2017) and using the detection, identification and adaptation (DIA) procedure to estimate errors caused by tropospheric delays (Ma and Verhagen 2020). Other researchers focused on using the tropospheric corrections from Numerical Weather Prediction (NWP) model in positioning techniques: studying the effect of NWP-based tropospheric corrections on PPP technique (Ibrahim and El-Rabbany 2011), applying tropospheric corrections from the European Center for Medium Range Weather Forecasts (ECMWF) in the PPP processing (Lu et al. 2016) and using tropospheric delays from NWP Weather Research and Forecasting (WRF) model (Wilgan et al. 2017). In addition to using NWP models, Yu et al. (2017) used voxel-based tomography results to improve the accuracy of the PPP technique.

The tropospheric tomography technique is a powerful and accurate approach for 4D reconstruction of water vapor. The first tropospheric tomography studies to obtain water vapor field were performed by Flores and Hirahara (Flores et al. 2000; Hirahara 2000). In the following years, many researchers have tried to optimize this technique (Bender et al. 2011; Rohm et al. 2014; Yao and Zhao 2016; Haji-Aghajany and Amerian 2017; Haji-Aghajany and Amerian 2018; Heublein et al. 2019; Haji-Aghajany et al. 2020a). A comprehensive overview of the advantages and deficiencies of current tomography models could be found in Brenot et al. (2020). Tropospheric tomography is generally done using the voxel-based approach. This method suffers from three disadvantages. First, the number of unknown parameters is high compared to the number of observations. Second, it needs empirical constraints in order to solve the rank deficiency of the coefficient matrix (Flores et

al. 2000; Rohm and Bosy 2009; Bender et al. 2011). These constraints sometimes divert the obtained results from the actual water vapor field. Third, generally the amount of water vapor is assumed to be constant in the 3D space of a voxel (Haji-Aghajany et al. 2020b). Recently, two new methods based on the polynomial and B-spline functions, called function-based tropospheric tomography approaches, have been proposed to overcome these drawbacks (Perler et al. 2011; Zhao et al. 2018; Haji-Aghajany et al. 2020b). Already in 2011, Perler et al. have demonstrated that tomographic methods based on polynomial functions allow to overcome these drawbacks (Perler et al. 2011). However, the impact on the PPP solution has not been studied so far. Thus, In this paper, the impact of using B-spline function-based and voxel-based tropospheric tomography methods on the accuracy and convergence time of the PPP solution in static and kinematic modes is investigated and the computed positions are compared with the positions obtained from empirical tropospheric correction models. For this purpose, a Global Positioning System (GPS) network in North America under different weather conditions is used. In the following, the basics of the PPP technique and tropospheric tomography methods are provided. Then, the study area and data set are presented and the configuration of the tomography models and the principles of GNSS processing are described. In the last section, the effect of tomography methods on the accuracy and convergence time of the PPP technique is validated.

2. PPP technique and tropospheric effect

The PPP is an approach that performs precise positioning in static or kinematic mode using a single GNSS dual frequency receiver and undifferenced code and carrier phase observations, along with precise GNSS orbit/clock products (Gao and Chen 2005). Therefore, it significantly reduces ground infrastructure costs and processing load. This method is capable of providing reliable and accurate position at sub-centimeter level for static positioning and sub-decimeter level for kinematic positioning. In static PPP, the receivers are motionless during the observation. In kinematic PPP, the receivers are either in periodic or continuous motion. This method is applied when real-time or near real-time results are needed (Zumberge et al. 1997; Gao 2006).

One of the nuisance effects on the GNSS signal is the delay caused by the signal passing through the ionosphere layer. This effect can be reduced significantly using the ionosphere-free combinations of dual-frequency GNSS observations (Heroux and Kouba 2001):

$$l_p = L + C(dt - dT) + T + \varepsilon_p \tag{1}$$

$$l_\varphi = L + C(dt - dT) + T + N\lambda + \varepsilon_\varphi \tag{2}$$

Where p is pseudoranges, φ is carrier-phase observations, l_p is the ionosphere-free combination of pseudoranges, l_φ is the ionosphere-free combination of carrier-phases, dt is the receiver clock offset, dT is the

satellite clock offset, C is the speed of signal in vacuum, T is the signal path delay due to the troposphere, N is the ambiguity of the carrier-phase, λ is the carrier wavelength, ε_φ and ε_p are the measurement noise components and L is the geometrical range.

Unlike the ionosphere delay, the tropospheric delay is independent of frequency and it is not possible to eliminate it by combination of two separate frequency signals. Over the years, various tools and methods have been proposed to estimate tropospheric delay. Radiosonde and water vapor radiometer (WVR) observations are among the most accurate information to correct for isotropic tropospheric delays. Another way is using empirical tropospheric models, e.g. Hopfield (1969) or Saastamoinen (1973) model together with a mapping function, e.g. Vienna Mapping Function (VMF1) (Böhm et al. 2008). These models are either based on long-term meteorological observations, forecast data or reanalysis data and are able to correct for tropospheric effects in GNSS signal processing. The third way is to consider tropospheric delay as unknown in the process of positioning. GNSS processing softwares like Bernese (Dach et al. 2015) and GAMIT (Herring et al. 2010) use this approach called general method. In this approach, the zenith tropospheric delay is considered as parameter and the hydrostatic delay from the empirical model is considered as an a priori value. In this paper, an alternative solution based on tomography methods is describe to further improve the accuracy and convergence time of positioning techniques is studied.

The GNSS processing has been done using Bernese software V.5.2. This is a high quality GNSS software that allows data processing in both static and kinematic modes using zero-difference and double-difference observables (Dach et al. 2015).

3. Tropospheric tomography concept

Slant water vapor (SWV) is one of the most widely used inputs in solving the tropospheric tomography problem. When this parameter is used as the input of the problem and to form the observation vector, the output of the tomography problem will be water vapor density (WVD) (Haji-Aghajany et al. 2020a):

$$SWV = \int_{\text{Rec.}}^{Sat.} \rho(s)ds \tag{3}$$

where ρ is the WVD and s indicates the path of the ray. Equation (3) is considered as the fundamental relation of the tropospheric tomography problem. The SWV is directly related to the slant wet delay (SWD) and it can be computed using the following formula (Bevis et al. 1992):

$$SWV = \frac{10^5}{R_w[(k_3/T_m)+k_2']}SWD \tag{4}$$

where $k_2^{'} = 16.48\ KhPa^{-1}$, $k_3 = 3.776 \times 10^5\ K^2 hPa^{-1}$ and $R_w = 461\ JKg^{-1}K^{-1}$ are refractivity coefficients. T_m is the weighted mean tropospheric temperature. Generally, the SWD is estimated using zenith wet delay (ZWD), non-hydrostatic delay gradients, non-hydrostatic mapping function, azimuth and satellite elevation (Davis et al. 1993).

3.1. Voxel-based method

In conventional tropospheric tomography, called voxel-based, the study area is divided into a large number of voxels. Therefore, Equation (3) can be rewritten as follows (Chen and Liu 2014):

$$SWV^P = \sum_{i}^{n} \sum_{j}^{m} \sum_{k}^{q} d_{i,j,k}^P \rho_{i,j.k} \tag{5}$$

where P is the counter of rays, n, m and q is the number of voxels in different directions, $d_{i,j.k}^P$ is the distance traveled by the ray P in voxel (i, j, k) and $\rho_{i,j,k}$ is the WVD.

3.2. Function-based method

The function-based tropospheric tomography uses only a few vertical layers and does not divide the tomography model in the horizontal direction (Zhao et al. 2018; Haji-Aghajany et al. 2020b). Based on this method the WVD for each vertical layer can be considered as a function of longitude (λ) and latitude (φ) of intersection between the ray and the center of the vertical layer. The SWV for P-th ray direction in i-th vertical layer can be expressed as:

$$SWV_i^P = \rho_i\, d_i^P = F_i(\lambda_i, \varphi_i)\, d_i^P \tag{6}$$

where ρ_i is the WVD for the location of (λ_i, φ_i) and d_i^P is the distance traveled by the P-th ray in the i-th layer. The spatial distribution of water vapor at various elevations is not the same. Therefore, it is necessary to use different degree functions for layers. Using Equation (6) the total SWD for P-th ray direction in n vertical layers can be written as follows:

$$SWV^P = F_1(\lambda_1, \varphi_1)\, d_1^P + F_2(\lambda_2, \varphi_2)\, d_2^P + \ldots + F_n(\lambda_n, \varphi_n)\, d_n^P \tag{7}$$

The general diagram of the function-based troposphere tomography method can be seen in Fig.1. The B-spline function is one of the most powerful functions in local modeling of various indicators. B-spline is a special kind of wavelet that provides important properties such as simplicity, semi-orthogonality, symmetry and compact support (Mautz et al. 2005; Amerian et al. 2013a,b). Therefore, the B-spline function is considered as the base function for local modeling of the water vapor. The normalized B-spline scaling function is written as (Amerian et al. 2013a,b; Haji-Aghajany et al. 2020b):

$$\phi_{J,k}(x) = N_{J,k}^{dg}(x) = \frac{x - t_k^J}{t_{k+dg}^J - t_k^J} N_{J,k}^{dg-1}(x) + \frac{t_{k+dg+1}^J - x}{t_{k+dg+1}^J - t_{k+1}^J} N_{J,k+1}^{dg-1}(x) \tag{8}$$

where *dg* is degree of function, *J* is resolution level, *k* is shift, *x* is variable and $t_0, t_1, ..., t_{K_J+dg}$ is a sequence of spaced values called knots. The B-spline scaling function space has $K_J = 2^J + dg$ basis functions. The 2D B-spline scaling function is calculated using the tensor product of 1D functions (Dahmen et al. 1980).

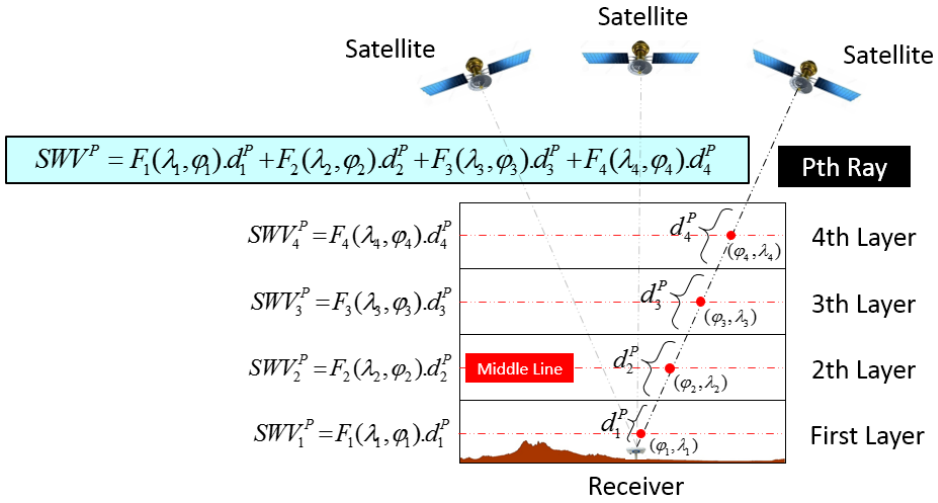

Figure 1. Schematic design of function-based tropospheric tomography (Haji-Aghajany et al. 2020b)

A 2D B-spline scaling function $\Phi_{J_1J_2k_1k_2}(\lambda,\varphi)$ with unknown scaling coefficients $C_{J_1J_2k_1k_2}$ is fitted to the WVD in each vertical layer:

$$\rho_i = \sum_{k_1=0}^{K_{J_1-1}} \sum_{k_2=0}^{K_{J_2-1}} C_{J_1J_2k_1k_2}\, \phi_{J_1J_2k_1k_2}(\lambda_i,\varphi_i) \tag{9}$$

The basic equation of the function-based tropospheric tomography based on 2D B-spline scaling function is as follows:

$$SWV^P = (d_1^P . \sum_{k_1=0}^{K_{J_1-1}} \sum_{k_2=0}^{K_{J_2-1}} C^1_{J_1J_2k_1k_2}\, \phi_{J_1J_2k_1k_2}(\lambda_1,\varphi_1)) + ... + (d_n^P . \sum_{k_1=0}^{K_{J_1-1}} \sum_{k_2=0}^{K_{J_2-1}} C^n_{J_1J_2k_1k_2}\, \phi_{J_1J_2k_1k_2}(\lambda_n,\varphi_n)) \tag{10}$$

This system of observations equations can be expressed in the following form:

$$L = A\,x \tag{11}$$

where *L* is the observation vector including SWV of each ray, *A* is the coefficient matrix including the base functions and distance traveled by the rays in each vertical layer, and *x* is a vector of unknowns including the B-spline scaling coefficients. This approach requires only vertical constraints, unlike the voxel-based tropospheric tomography. More details about the function-based tropospheric tomography can be studied in Haji-Aghajany et al. (2020b).

The tropospheric tomography is a kind of Fredholm integral equation, so it is an ill-condition problem (Hansen 1997). In this paper, the Least-Squares QR (LSQR) iterative regularization approach is considered to solve the tropospheric tomography problem (Hansen 1997). It should be noted that the 3D ray-tracing technique is applied to calculate the distance traveled by the rays in each vertical layer (Haji-Aghajany and Amerian, 2017; Haji-Aghajany et al., 2019). More details about this technique and its applications in different fields of geodesy and remote sensing can be found in Haji-Aghajany and Amerian (2017), Möller and Landskron (2019) and Haji-Aghajany and Amerian (2020).

4. Study area and data set

In this paper, an area in North America has been selected to investigate the effect of the tropospheric tomography methods on the accuracy and convergence time of the PPP technique (Fig.2). Topography of the study area and the horizontal and vertical distributions of the Plate Boundary Observatory (PBO) GNSS stations network (https ://unavc o.org). stations are visible in Fig.3. In order to conduct comprehensive study 30 Days from varoius months of Year (DOYs) 2018 under different conditions including standard and more dynamic weather have been processed.

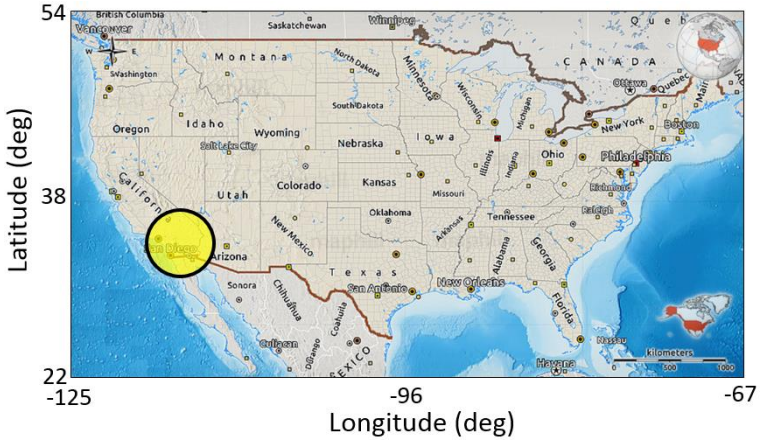

Figure 2. Geographical location of the study area (yellow circle)

The climate reanalysis dataset is one of the most important products of the ECMWF. The advantages of using this data in various fields such as geodesy, remote sensing and atmospheric modeling has been investigated in previous researches (Douša, and Eliaš., 2014; Jolivet et al., 2014; Haji-Aghajany et al., 2017). In this study, the ERA-Interim reanalysis data that provided values of several meteorological data on 37 pressure levels with a spatial resolution of about 75 km and a temporal resolution of 6 hours has been used to run the 3D ray tracing technique and the empirical models (Dee et al., 2011). The bilinear and spline techniques have been used for spatial and temporal interpolation, respectively.

Before studying the effect of function-based tropospheric tomography on the PPP technique, the reconstructed water vapor fields are evaluated with observations of the only radiosonde station EDW located in the study area. Radiosonde balloons are generally launched twice a day at 00:00 and 12:00 UTC.

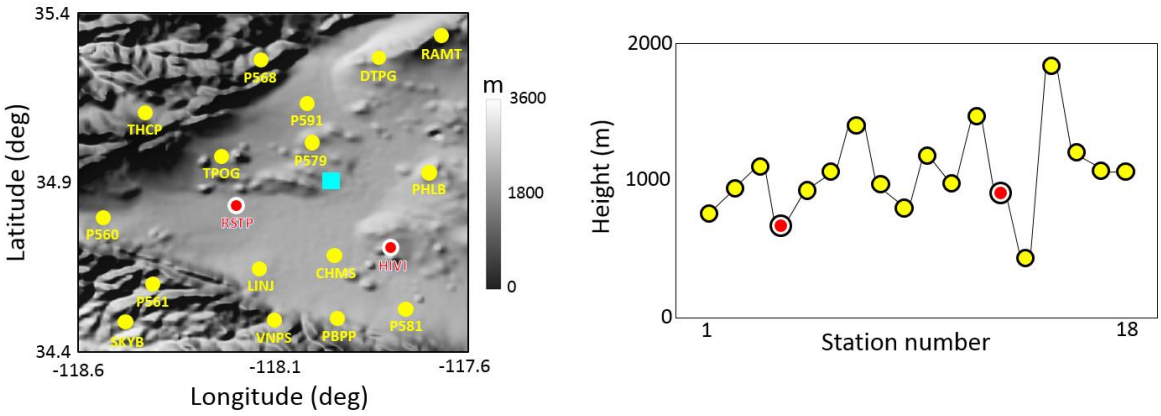

Figure 3. Horizontal and vertical distributions of GNSS stations. The red circles indicate the stations RSTP and HIVI that are considered to study the effect of tomography on the PPP technique. The blue square shows the location of the radiosonde station

5. Processing and configuration

5.1. GNSS signal processing

In this paper, positioning parameters to calculate the tropospheric delay as input to the tomography methods have been considered based on the Table 1. Two stations of the network have been considered as validation stations to investigate the effect of different tropospheric correction methods on the PPP technique. Fig.4 represents a sample of the time series of the position components of these stations. These time series have been obtained from the PBO analysis center. In order to check the results, we have estimated a reference position by fitting a line to the time series results. An example of the obtained equations from the fitted lines can be seen in Table 2. This process has been done separately for each month of 2018.

Table 1. Bernese processing parameters

Parameter	model
Satellite orbit and clock ephemeris	CODE (15 min)
Differential code biases (DCB)	IGS
Earth Rotation Parameters	CODE
Satellite phase center offsets	PCV.I14
Receiver phase center offsets	PCV.I14

Ionospheric model	Linear ionospheric free combination
Atmosphere estimation	Gradient estimation model: Chenher 6 hours (Chen and Herring, 1997) Absolute and relative constraint: 5 m Temporal resolution of ZTD: 1 hour
GNSS system	GPS
Observation type	Phase and code
Ocean tidal loading	FES2004 (Lyard et al. 2006)
Atmosphere tidal loading	Ray-Ponte (Ray and Ponte, 2003)
Cut-off angle	10 degrees

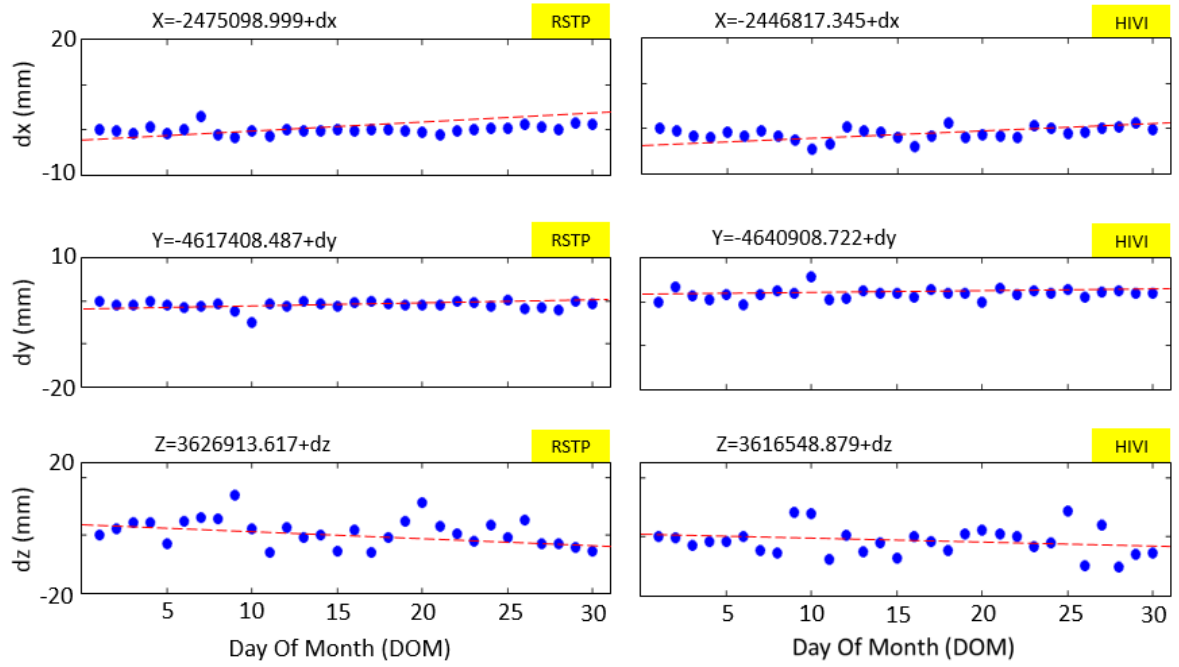

Figure 4. Position time series of the stations RSTP and HIVI and fitted lines in January 2018

Table 2. The equations of the fitted lines in January 2018

Station	X (m)	Y (m)	Z (m)
RSTP	-2475098.999 + $(0.03046\times DOM-0.4641)\times10^{-3}$	- 4617408.487 + $(0.00822\times DOM-1.059)\times10^{-3}$	3626913.617 + $(-0.1702\times DOM+3.909)\times10^{-3}$
HIVI	-2446817.345 + $(0.05287\times DOM-1.957)\times10^{-3}$	-4640908.722 + $(0.02648\times DOM+1.458)\times10^{-3}$	3616548.879 + $(-0.08669\times DOM-0.2283)\times10^{-3}$

5.2. Tomography model configuration

In order to comprehensively study the effect of tropospheric tomography on the accuracy and convergence time of the PPP technique, both types of tomography methods, including function-based and voxel-based have been performed. Based on the previous researches, the optimal horizontal resolution of the voxel-based tomography model has been computed based on the resolution matrix. The model resolution matrix is one of the features of the coefficient matrix and reflects the resolution and geometry of the tomography model. If any of the diagonal elements of this matrix are trivial, the relevant parameters will be estimated poorly. An optimal design of the tomography model results in a resolution matrix which is close to identity (Bender et al. 2011; Haji-Aghajany and Amerian 2017; Adavi and Weber 2019). The horizontal resolution of 0.2 degree has been selected for the voxel-based tomography model based on the topography of the area and thickness of the vertical layers that increases with height (Fig.5).

In order to build the function-based tropospheric tomography model, the vertical resolution has been considered in accordance with the vertical resolution of the voxel-based model (Fig.5).

As the spatial variation of water vapor decreases with increasing height, different degrees and levels of B-spline function must be used in various vertical layers. Selecting the optimal degree of function in each vertical layer is one of the most important steps in function-based tomography. For this purpose, the B-spline functions with different degrees and levels have been fitted to one year of ERA-Interim data, and the coefficients of the B-spline functions have been calculated under different weather conditions and different average relative humidity. Finally, the optimal degrees and levels of the B-spline function in each vertical layer have been selected based on these processes.

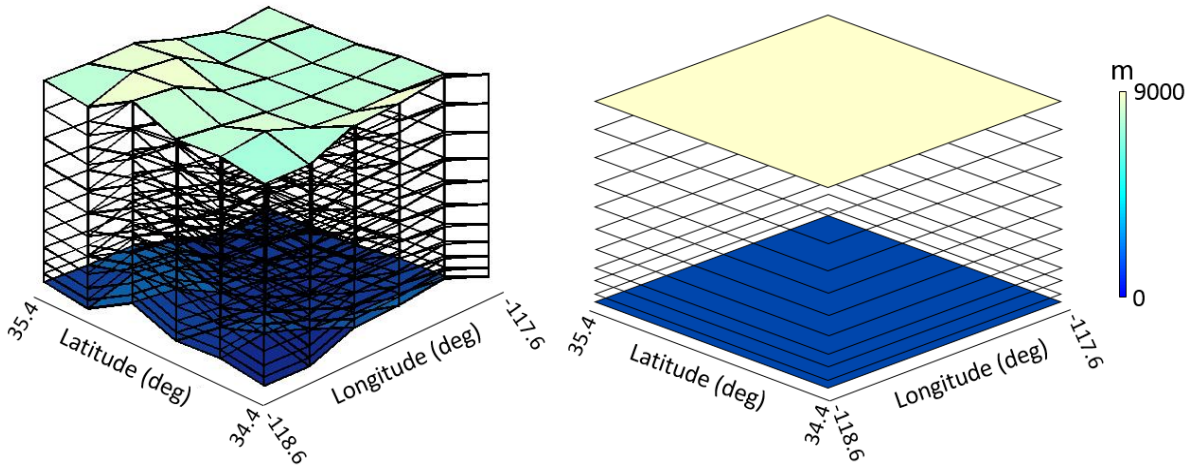

Figure 5. Voxel-based (left) and function-based (right) tomography models

5.3. Tropospheric correction

As mentioned, the purpose of this paper is to investigate the effect of different tropospheric correction methods on the positioning accuracy. Therefore, estimating the tropospheric delay using the mentioned methods and applying them to the observations can be considered as the most important processing steps. The first approach is to use tropospheric corrections obtained from tomography methods. In the first step, the ZTD has been extracted from GPS processes based on the parameters specified in the Table 1. The ZWD has been estimated by subtracting ZHD calculated by the Saastamoinen model from the ZTD. The ERA-Interim data has been used to perform Saastamoinen model.

In the next step, the SWD has been projected along the line of sight (LOS) of the satellites using the Global Mapping Function (GMF) (Böhm et al. 2006). Subsequently, the SWV obtained from the SWD has been considered as the input of tomography methods. After performing troposphere tomography, the reconstituted water vapor has been used as the input of the 3D ray tracing technique to calculate the tropospheric delay. The calculated delays have been applied to the observations of the Receiver INdependent EXchange (RINEX) files and the corrected files has been entered into the software.

The second method of estimating the tropospheric delay is to use the Saastamoinen model. This model requires tropospheric indices at the surface level. The calculated tropospheric delay is projected along the LOS using the GMF.

The third method is to use the tropospheric delays and gradients published by the VMF group and project them along the LOS direction using the VMF1 mapping function. The obtained tropospheric delays are set in the form of a TRP file and introduced to the software (Dach et al. 2015).

In the last approach, called the general method, the tropospheric delay and its gradients are considered as unknowns and are estimated along with other parameters. In this method, the dry GMF model where ZTD corrections are computed based on Global Pressure Temperature model (GPT) has been used as the priori value of the tropospheric delay (Böhm et al. 2007).

6. Results and discussion

6.1. Evaluation of tomography results

Before applying tomography results based on the mentioned configurations on positioning techniques, it is necessary to evaluate these results using the radiosonde observations located in the study area. Fig.6 indicates the obtained WVD from tomography at four sample epochs. In order to evaluate the results, the reconstructed

water vapor fields have been compared with radiosonde observations for 30 days from different months of 2018. Examples of this comparison for two epochs can be seen in Fig.7 and Fig.8. This comparison shows that at the lower and middle vertical layers, the differences between the obtained water vapor fields from the two methods and the radiosonde data are higher than at upper layers, although in general the trend of the variations of the obtained WVD are consistent with the validation data. In other words, the increasing or decreasing trend of obtained WVD is similar to radiosonde data. Table 3 shows the statistical parameters between the results of tropospheric tomography methods and radiosonde data over the test period.

The calculated statistical results show that the use of the function-based approach reduces the average root mean square error (RMSE) from 0.86 gr/m^3 to 0.45 gr/m^3. After confirming the results obtained from tropospheric tomography, the GPS observations have been corrected using the reconstructed water vapor fields. In the next section, the effect of tomography on the PPP technique is examined.

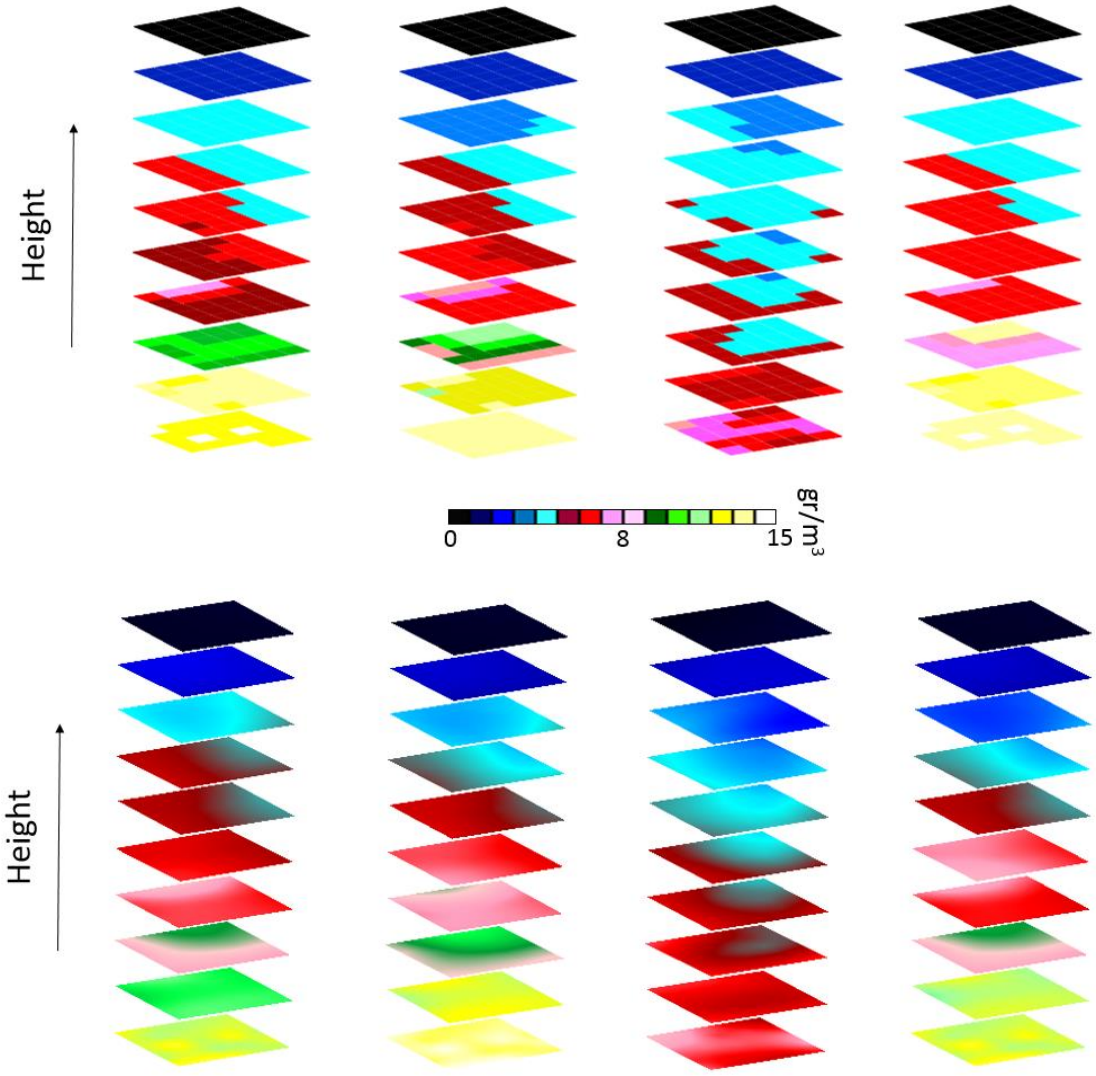

Figure 6. WVD fields obtained using voxel-based (up) and function-based (down) tropospheric tomography approaches (From left to right: 20181004 (6 AM), 20181004 (12 PM), 20180705 (6 AM), 20180705 (12 PM)).

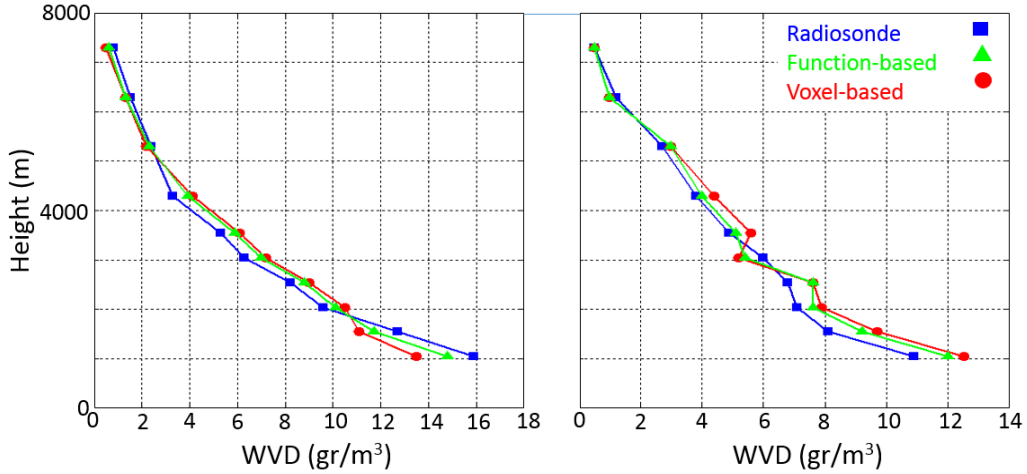

Figure 7. Comparison between reconstructed water vapor and radiosonde data (left panel: 20181004, right panel: 20180705)

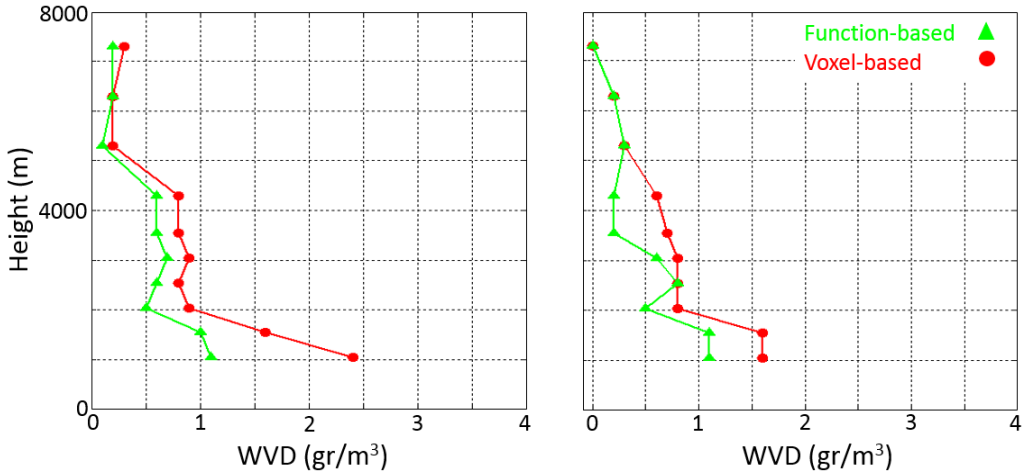

Figure 8. Absolute values of the difference between the obtained WVD and radiosonde measurements (left panel: 20181004, right panel: 20180705)

Table 3. Statistical comparison between the reconstructed WVD and radiosonde validation data during the test period (30 days from different months of 2018)

Method	RMSE (gr/m^3)	Bias (gr/m^3)	Min-Diff (gr/m^3)	Max-Diff (gr/m^3)
Function-based	0.41	-0.11	0.09	0.81
Voxel-based	0.86	-0.16	0.14	1.41

6.2. Static PPP mode

In order to conduct a comprehensive study, the static PPP has been performed using four correction methods including general approach, Saastamoinen model, VMF1 mapping functions and tomography results. Fig.9 shows the obtained error in estimating the position components of the two stations RSTP and HIVI during the 30 days from different months of 2018. In order to better compare the ability of the methods, the statistical

results of the obtained positions are presented in Table 4. The maximum difference between the RMSE of the general, Saastamoinen and VMF1 methods is about 0.31 cm. The maximum of about 6 cm error obtained from these approaches is related to the up component. The use of tomography models has significantly reduced the error of the position components. The maximum error in tomography methods of about 5 cm is observed in the up component. On many days, the error obtained from the function-based method and the voxel-based approach is close. However, on some days with wet weather conditions, the difference between the results of the two methods is significant, and the use of the function-based tomography has led to more accurate positions. In computing the up component, the general method provides better accuracy than the Saastamoinen model and VMF1 method. In addition, the greater ability of the function-based method compared to the voxel-based approach can be proved based on these statistical results as the function-based tomography has been able to increase the accuracy of the up component by up to half a centimeter compared to the voxel-based method. In general, the use of tomography has a significant effect on increasing the accuracy of 3D coordinates. Finally, it can be said that the function-based tomography is an appropriate way to model and reduce the effect of the troposphere on the position, especially on the up component in static PPP mode.

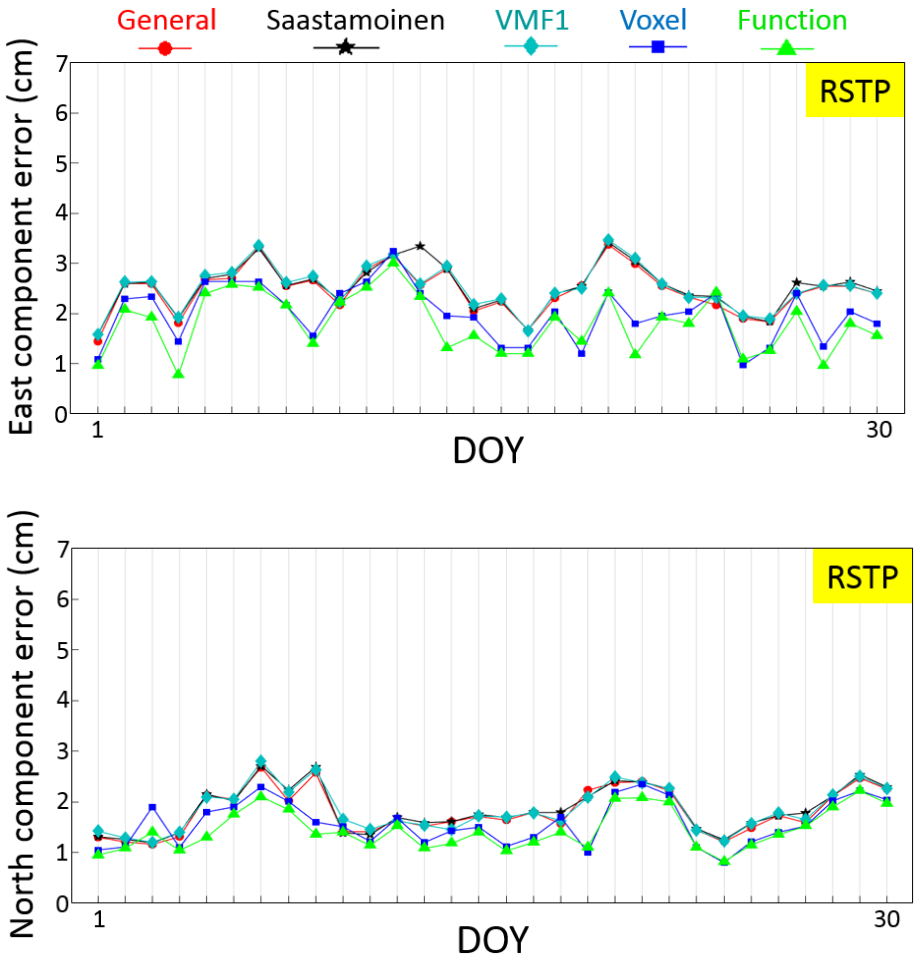

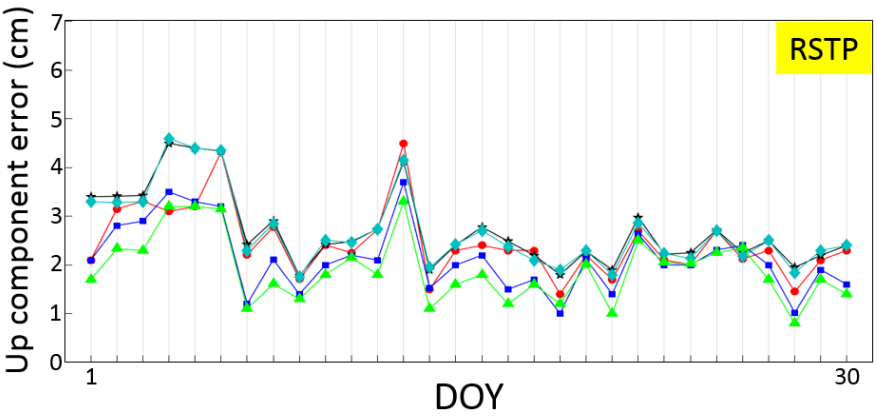
RSTP
Up component error (cm)
0
1
2
3
4
5
6
7
1
30
DOY

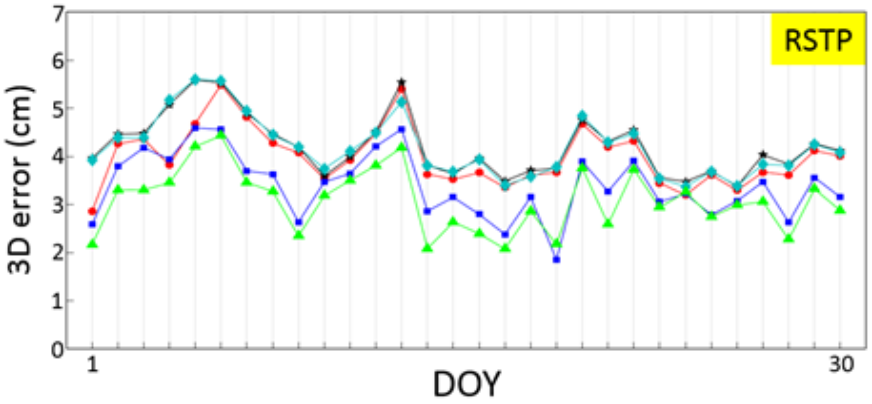
RSTP
3D error (cm)
0
1
2
3
4
5
6
7
1
30
DOY

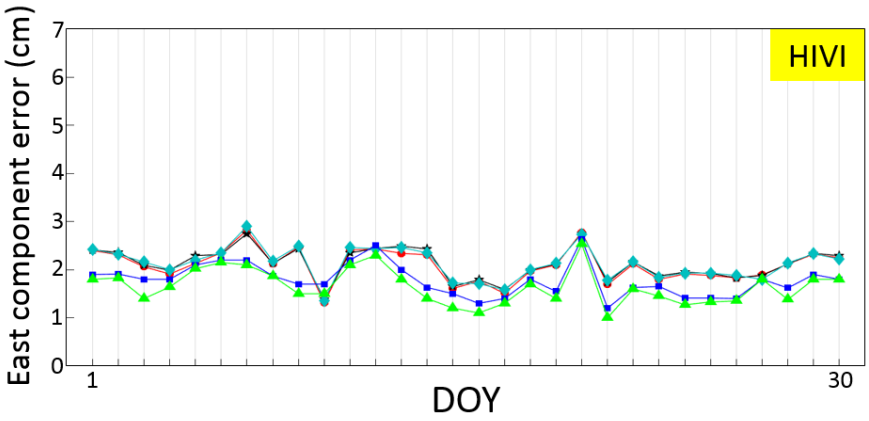
HIVI
East component error (cm)
0
1
2
3
4
5
6
7
1
30
DOY

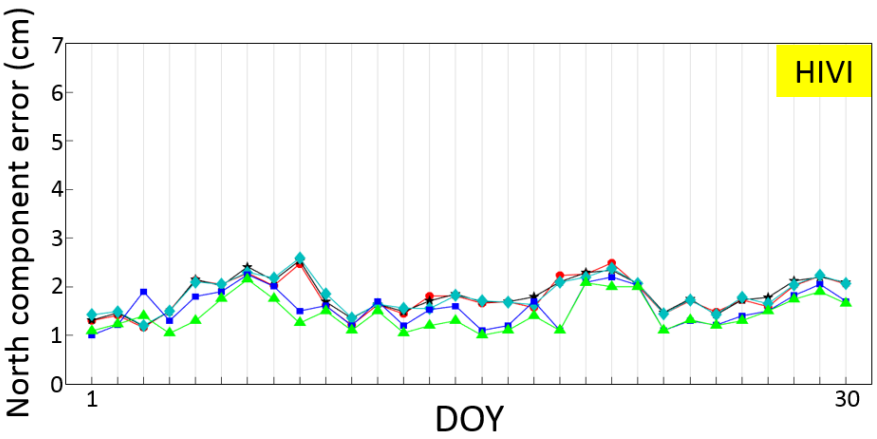
HIVI
North component error (cm)
0
1
2
3
4
5
6
7
1
30
DOY

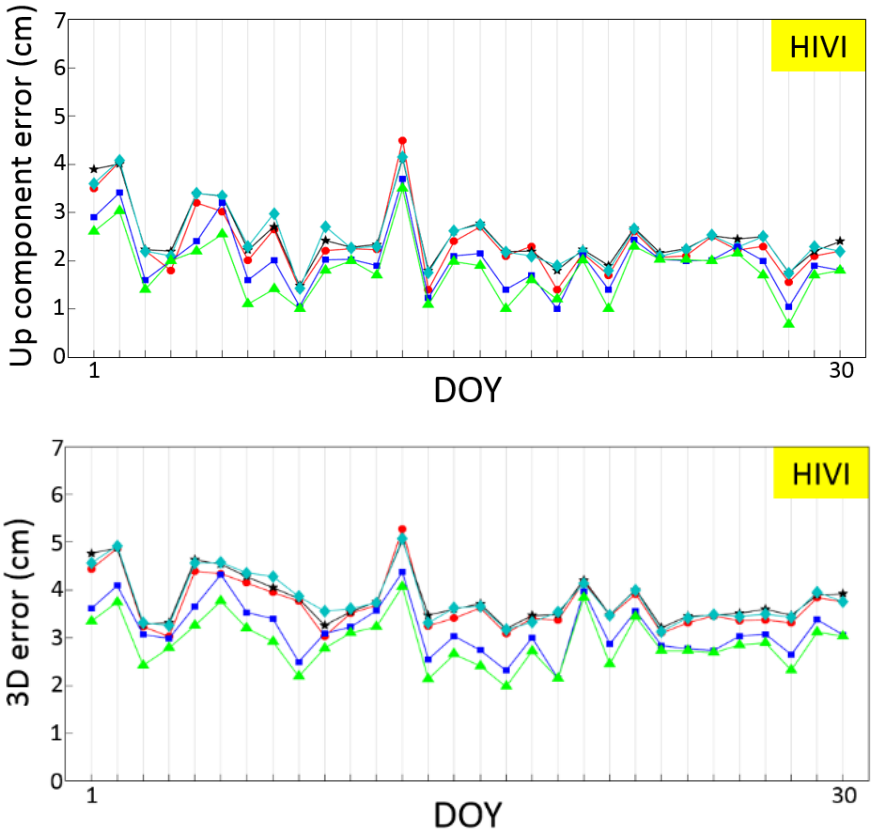

Figure 9. Static PPP results at two stations RSTP and HIVI using different correction methods

Table 4. Statistical results for the static PPP using different correction methods

Station	Method	East RMSE (cm)	North RMSE (cm)	Up RMSE (cm)
RSTP	General	1.63	1.23	2.53
	Saastamoinen	1.69	1.27	2.74
	VMF1	1.68	1.23	2.71
	Voxel-based	1.22	1.18	2.12
	Function-based	1.09	1.12	1.70
HIVI	General	1.58	1.48	2.55
	Saastamoinen	1.89	1.55	2.73
	VMF1	1.74	1.50	2.60
	Voxel-based	1.33	1.28	1.57
	Function-based	1.27	1.24	1.51

6.3. Kinematic PPP mode

It is expected that the effect of using the various correction methods in kinematic mode will be higher than in static mode. In this paper, based on the obtained results from kinematic solution, it is assumed that the positions obtained are convergent when the error of each component is less than 15 cm. PPP technique in kinematic mode

requires an initial time to converge. Based on the processing, it was observed that this time is about four hours. Thus, the first four hours of processing have been removed from the calculations and have not been analyzed. In this mode, in addition to examining the results of using the mentioned tropospheric correction methods, the effect of using the conventional kinematic positioning is also studied. In the conventional method, called classic, tropospheric corrections are estimated in adjacent stations and transferred to the desired station using interpolation methods. In this paper, spline interpolation has been used for this purpose (Sadikin et al. 2017). Fig.10 indicates the kinematic coordinate errors at two stations on one of the test days. The probability diagram of the position components during the test period is presented in Fig.11. In order to better evaluate the correction methods, the statistical results of the estimated positions are shown in Table 5. Tomography methods have had a significant effect on increasing the accuracy of the east and up components, although their use has not had much effect on the north component. Fig.10 shows also that the function-based troposphere tomography method had more power to increase the accuracy of the position. There is a difference of more than 1 cm between the results of the function-based and the voxel-based methods at some epochs.

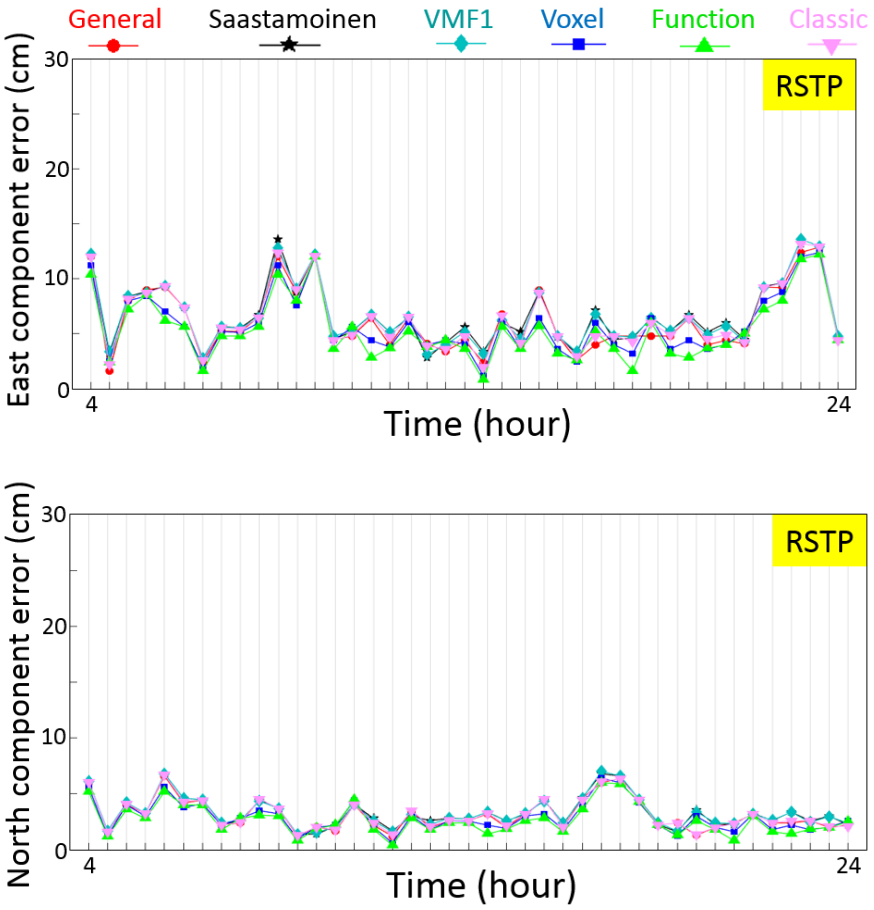

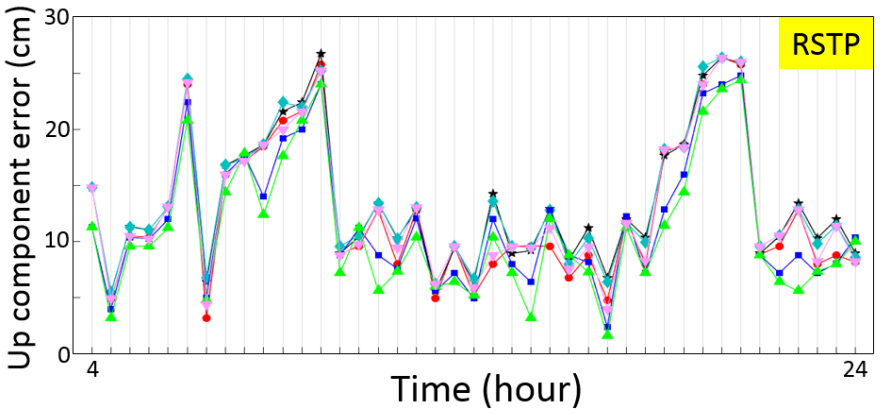
RSTP
Up component error (cm)
30
20
10
0
4
24
Time (hour)

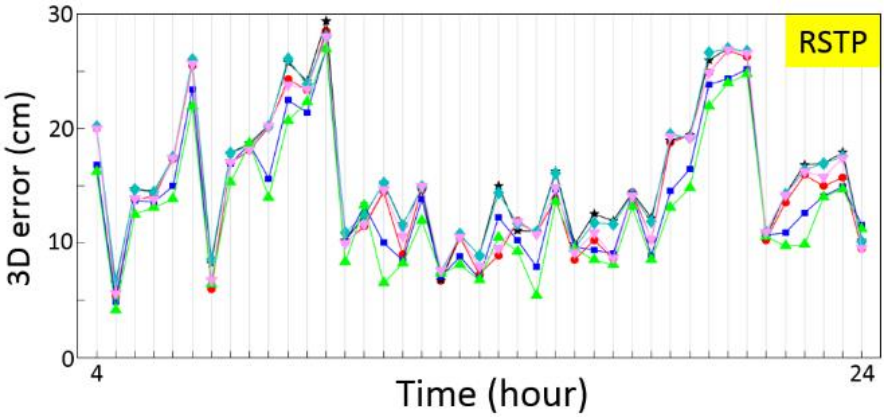
RSTP
3D error (cm)
30
20
10
0
4
24
Time (hour)

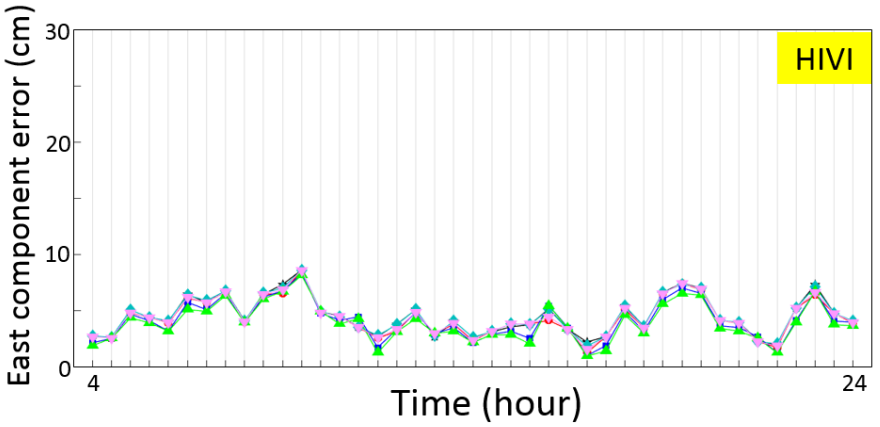
HIVI
East component error (cm)
30
20
10
0
4
24
Time (hour)

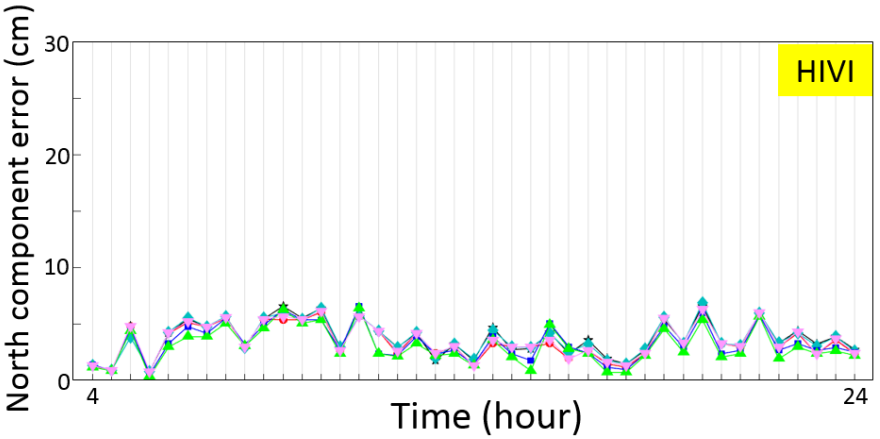
HIVI
North component error (cm)
30
20
10
0
4
24
Time (hour)

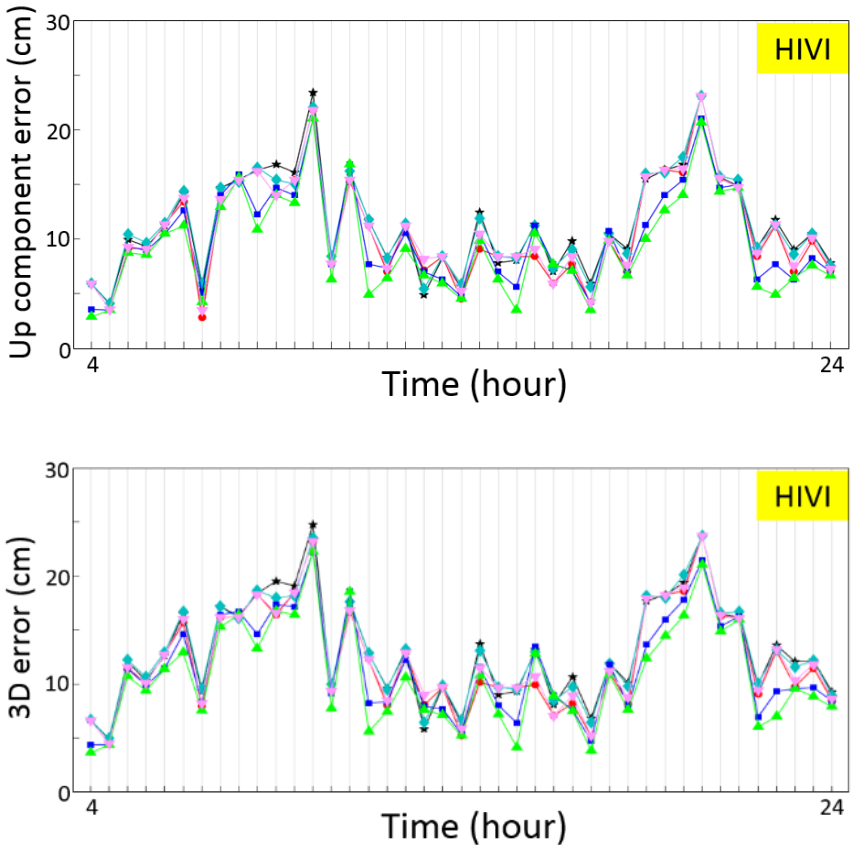

Figure 10. Kinematic PPP results at two stations RSTP and HIVI using correction methods on one of the test days (20181004)

Based on Fig.11, it can be said that the classic, general, Saastamoinen and VMF1 approaches have higher probability of larger error than the tomography methods in east and up components.

In order to make a comprehensive comparison, it is necessary to use the statistical results presented in Table 5. The highest and lowest RMSE in estimating the east component is related to the Saastamoinen and function-based tomography methods, respectively. The classic and general methods have worked better than the VMF1 and Saastamoinen approaches.

The difference among the results of the classic approach, general method and the voxel-based tomography is very small, about 3 mm. The function-based tomography has been able to increase the accuracy of the voxel-based method by about 5 mm. Similar to the east component, the power of the classic and general methods in calculating the north component is higher than the Saastamoinen and VMF1 approaches, although their differences are not significant at all. The use of tomography methods has not been able to remarkably improve the accuracy compared to the general approaches. The RMSE from the function-based tomography method is 3.03 and 3.21 mm, while the RMSE of the voxel-based approach is about 3.13 and 3.51 mm for each station.

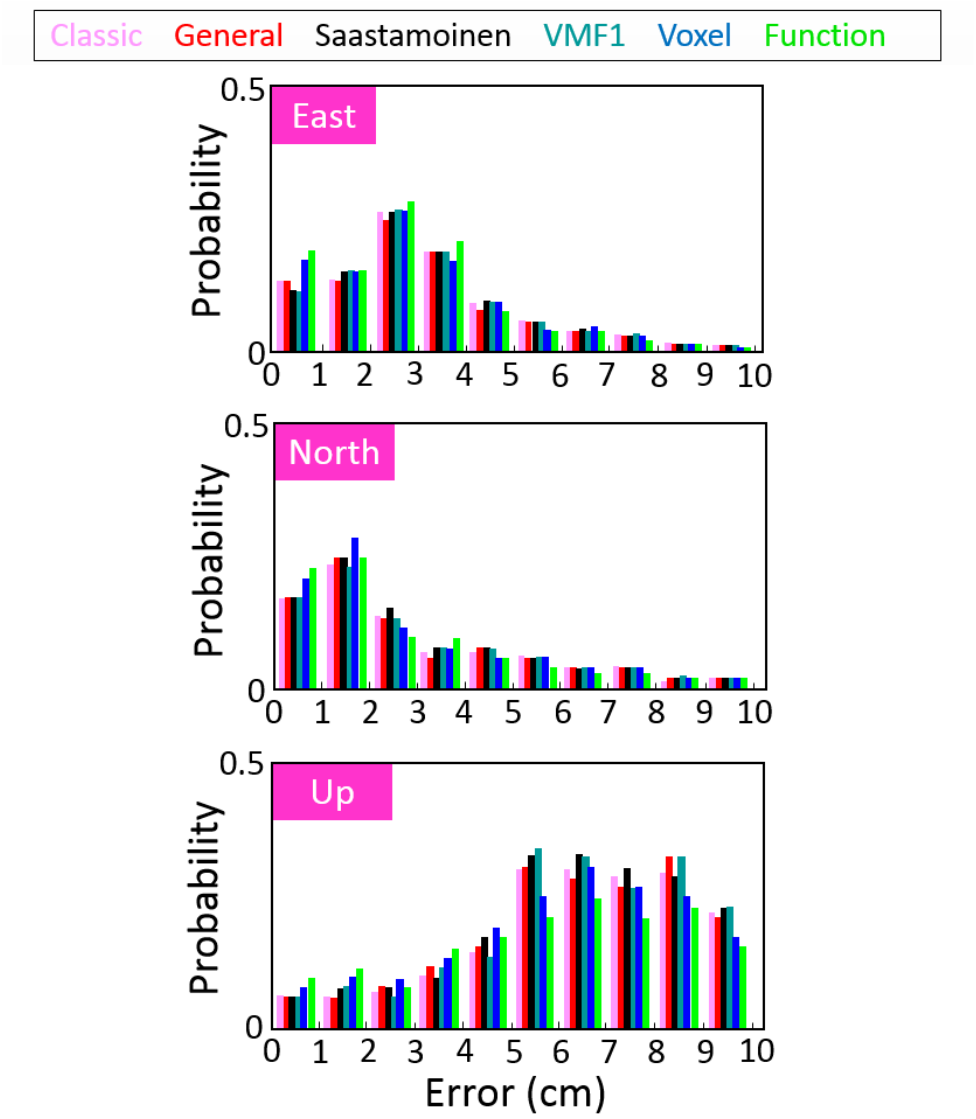

Figure 11. Probability diagram of the position components derived from two stations RSTP and HIVI over the test period

The difference between the estimated RMSE in the calculation of the up component is significant. Again, the classic and general methods performed better than the Saastamoinen and VMF1 models. However, this time the difference between the classic and general approaches and the other two methods cannot be ignored. The use of voxel-based tomography has reduced the RMSE of the up component by about 2.39 and 1.22 cm for each station compared to the general method.

The most important statistical results is that the function-based tomography has been able to increase the accuracy of the up component by 0.79 and 0.71 cm more than the voxel-based method. Generally, it can be said the function-based tomography improve the accuracy of the kinematic PPP in the east component compared to the voxel-based tomography. However, the use of different tropospheric correction methods in computing the

north component has similar results. The obtained RMSEs show that the use of function-based tomography method has a very important role in increasing the accuracy of the kinematic PPP.

Table 5. Average statistical results for the kinematic PPP using correction methods during the test period

Station	Method	East RMSE (cm)	North RMSE (cm)	Up RMSE (cm)
RSTP	General	6.02	3.26	12.05
	Classic	6.11	3.29	12.18
	Saastamoinen	6.35	3.45	12.61
	VMF1	6.31	3.44	12.53
	Voxel-based	5.85	3.13	9.66
	Function-based	5.34	3.03	8.87
HIVI	General	4.51	3.83	10.33
	Classic	4.59	3.87	10.71
	Saastamoinen	4.63	4.97	10.95
	VMF1	4.61	3.92	10.74
	Voxel-based	4.31	3.51	9.11
	Function-based	4.01	3.21	8.41

6.4. Convergence time

After studying the effect of using different tropospheric correction methods on the accuracy of the PPP technique in different modes, it is necessary to check the effect of these methods on the convergence time of the kinematic PPP solution. Fig.12 indicates the convergence time of the kinematic PPP technique. Table.6 presents the average of convergence times for each station and method during the 30 days from different months of 2018. In general, the tomography methods have a shorter convergence time in all components of the two stations. Longest convergence time is related to the general method, which is significantly different from the other approaches in some cases. The shortest convergence time is related to the function-based tomography, which in some cases has caused an increase in processing speed. For the east component, the function-based method at station RSTP improved the convergence time by about 9% compared to the voxel-based method. For the up component, the function-based method has decreased the convergence time by about 6% and 8% at the two stations. For the north component, he results obtained from the two tomography methods are similar at both stations.

Generally, it can be assumed that using function-based tomography results might help to accelerate the convergence time. Using the tomography method can help further to reduce the convergence time of all components compared to the voxel-based method.

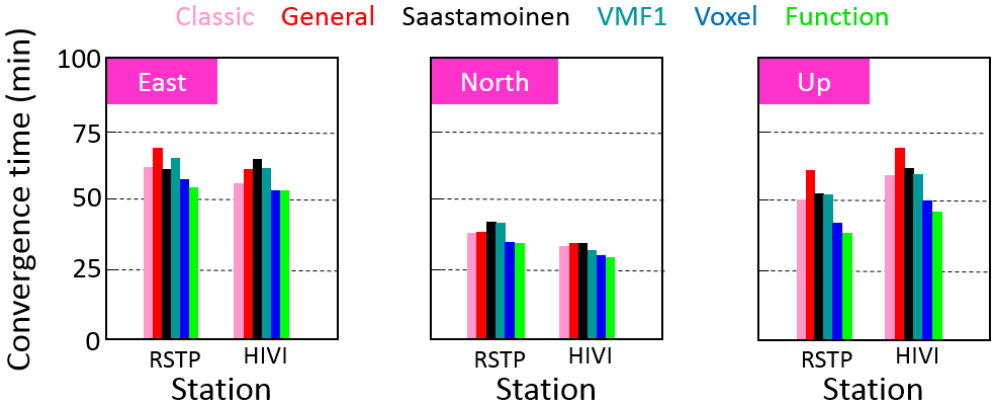

Figure 12. Average convergence times of kinematic PPP during the test period

Table 6. Average of convergence times for each method during the test period of kinematic PPP

Station	Method	East (min)	North (min)	Up (min)
RSTP	Classic	63	37	49
	General	68	38	59
	Saastamoinen	59	39	51
	VMF1	65	39	51
	Voxel-based	56	33	44
	Function-based	52	33	41
HIVI	Classic	55	32	56
	General	59	33	69
	Saastamoinen	65	33	60
	VMF1	59	30	58
	Voxel-based	52	29	50
	Function-based	52	28	46

7. Conclusion

In this paper, the effect of using the function-based tropospheric tomography method in increasing the accuracy and convergence rate of the PPP technique was investigated. For this purpose, the observations of a GNSS network were processed over a long time period and under different weather conditions.

In order to conduct a comprehensive study, the results of using the function-based tomography method were compared with the results of other approaches, including general, Saastamoinen and VMF1 models and voxel-

based tomography. The results obtained from these methods were also evaluated using the observations of a radiosonde station. Validation results showed that the function-based tomography is more accurate than the voxel-based tomography in water vapor reconstruction. Then, the effect of these methods on the accuracy of the static PPP solution was studied. The results showed that the function-based tomography leads to more accurate positions compared to other methods, especially in the east and up component. Then, the effect of using different tropospheric correction methods in the kinematic PPP solution was investigated. Again, the results showed that the function-based tomography has the best performance in estimating the east and up components of the position. In order to complete this study, convergence time in kinematic PPP mode was also checked. Based on the results, it was found that the function-based tomography reduces the convergence time of all components compared to other tropospheric correction approaches. This paper is mainly dedicated to demonstrate to the methodology of the various approaches and their initial comparison. In a next study more comparison for more GNSS stations in various regions of the world will follow.

Acknowledgments

Authors would like to appreciate the UNAVCO for the GPS observations. We are also grateful to the ECMWF for publishing ERA-Interim data.

Author contributions

S.H-A,Y.A and W.R conceptualized the study. S.H-A and Y.A processed data and prepared the paper draft. S.V, H.S and W.R substantially contributed to the interpretation of results and provided many useful suggestions in the internal review process. All authors were involved in result discussions throughout the development.

Data availability statement

All the GPS data used in this paper are publicly available in the UNAVCO data portal (https://www.unavco.org/data/gps-gnss/data-access-methods/dai2/app/dai2.html). The reanalysis data, ERA-Interim product, are released by ECMWF at https://www.ecmwf.int/.

References

Adavi, Z. and Weber, R.: Evaluation of Virtual Reference Station Constraints for GNSS Tropospheric Tomography in Austria Region, Adv. Geosci., 50, 39-48, https://doi.org/10.5194/adgeo-50-39-2019, 2019.

Amerian Y, Hossainali MM, Voosoghi B (2013a) Regional improvement of IRI extracted ionospheric electron density by compactly supported base functions using GPS observations. J Atmos Sol Terr Phys 92:23–30. doi: 10.1016/j.jastp.2012.09.011.

Amerian Y, Voosoghi B, Mashhadi Hossainali M (2013b) Regional Ionosphere Modeling in Support of IRI and Wavelet Using GPS Observations. Acta Geophysica. 61(5):1246-1261, DOI: 10.2478/s11600-013-0121-5.

Bender M, Stosius R, Zus F, et al (2011) GNSS water vapour tomography – Expected improvements by combining GPS, GLONASS and Galileo observations. Adv. Space Res. 47, 886-897.

Bevis M, Businger S, Herring T A, Rocken C, Anthes R. A, Ware R H (1992) GPS meteorology: Remote sensing of atmospheric water vapor using the Global Positioning System. Journal of Geophysical Research: Atmospheres, 97(D14), 15787-15801.

Brenot H, Rohm W, Kačmařík M, Möller G, Sá A, Tondaś D, Champollion C (2020) Cross-Comparison and Methodological Improvement in GPS Tomography. Remote Sensing, 12(1), 30.

Böhm, J., A. Niell, P. Tregoning, and H. Schuh. Global Mapping Function (GMF): A new empirical mapping function based on numerical weather model data. Geophysical Research Letters, 33 (7):L07304, 2006. doi: 10.1029/2005GL025546.

Böhm, J., R. Heinkelmann, and H. Schuh. Short Note: A global model of pressure and temperature for geodetic applications. Journal of Geodesy, 81(10):679–683, 2007. doi:10.1007/s00190-007-0135-3.

Böhm, J, Kouba J, Schuh H (2008) Forecast Vienna Mapping Functions 1 for real-time analysis of space geodetic observations. J. Geodesy 83, 397–401.

Chen, G. and T. A. Herring. Effects of atmospheric azimuthal asymmetry on the analysis of space geodetic data. Journal of Geophysical Research, 102(B9):20489–20502, 1997. doi: 10.1029/97JB01739.

Chen BY, Liu ZZ (2014) Voxel-optimized regional water vapor tomography and comparison with radiosonde and numerical weather model. J Geod 88:391–703. doi:10.1007/s00190-014- 0715-y.

Dach R, S Lutz, P Walser, P. Fridez (2015) Bernese GNSS Software Version 5.2. User manual, Astronomical Institute, University of Bern, Bern Open Publishing. DOI: 10.7892/boris.72297; ISBN: 978-3-906813-05-9.

Dahmen W, DeVore R, Scherer K, Multi-Dimensional Spline Approximation, SIAM J. Numer. Analy. 17 (3) (1980) 380–402

Davis J, Elgered G, Niell A E, C E Kuehn (1993) Ground-based measurement of gradients in the wet radio refractivity of air. Radio Sci., vol. 28, pp. 1003–1038.

Dee D.P., et al (2011) The ERA-Interim reanalysis: configuration and performance of the data assimilation system, Q. J. R. Meteorol. Soc. 137(656): 553–597, doi: 10.1002/qj.828.

Douša, J., & Eliaš, M. (2014). An improved model for calculating tropospheric wet delay. Geophysical Research Letters, 41. https://doi.org/10.1002/2014GL060271.

Flores A, Ruffini G, Rius A (2000) 4D tropospheric tomography using GPS slant wet delays, Ann. Geophys. Ger., 18, 223–234.

Gao Y, Chen K (2005) Performance analysis of precise point positioning using real-time orbit and clock products. J. Glob. Position. Syst. 3, 95–100.

Gao Y (2006) GNSS solutions: Precise point positioning and its challenges. Inside GNSS November/December, 16–18.

Hadas T, Kaplon J, Bosy J, Sierny J, Wilgan K (2013) Near-real-time regional troposphere models for the GNSS precise point positioning technique. Meas. Sci. Technol. 24, 055003.

Haji-Aghajany S, Voosoghi B, Yazdian A (2017) Estimation of north Tabriz fault parameters using neural networks and 3D tropospherically corrected surface displacement field. Geomat. Nat. Hazards Risk 8, 918–932.

Haji-Aghajany S, Amerian Y (2017) Three dimensional ray tracing technique for tropospheric water vapor tomography using GPS measurements. Journal of Atmospheric and Solar-Terrestrial Physics. 164, 81-88. doi: 10.1016/j.jastp.2017.08.003.

Haji-Aghajany S, Amerian Y (2018) Hybrid Regularized GPS Tropospheric Sensing Using 3-D Ray Tracing Technique. IEEE Geoscience and Remote Sensing Letters. 15, 1475-1479. doi: 10.1109/LGRS.2018.2853183.

Haji-Aghajany S, Voosoghi B, Amerian Y (2019) Estimating the slip rate on the north Tabriz fault (Iran) from InSAR measurements with tropospheric correction using 3D ray tracing technique. Adv. Space Res. 64, 2199–2208.

Haji-Aghajany S, Amerian Y, (2020) Atmospheric phase screen estimation for land subsidence evaluation by InSAR time series analysis in Kurdistan, Iran. Journal of Atmospheric and Solar-Terrestrial Physics. https://doi.org/10.1016/j.jastp.2020.105314.

Haji-Aghajany S, Amerian Y, Verhagen S, Rohm W, Ma H (2020a) An Optimal Troposphere Tomography Technique Using the WRF Model Outputs and Topography of the Area. Remote Sens. 12, 1442. https://doi.org/10.3390/rs12091442.

Haji-Aghajany S, Amerian Y, Verhagen S (2020b) B-spline function-based approach for GPS tropospheric tomography. GPS Solut 24, 88. https://doi.org/10.1007/s10291-020-01005-x.

Hansen P C (1997) Rank-deficient and Discrete Ill-posed Problems. Numerical Aspects of Linear Inversion, Monographs on Mathematical Modeling and computation, Vol. 4, SIAM, Philadelphia.

Heroux P, Kouba J (2001) GPS precise point positioning using IGS orbit products. Phys. Chem. Earth, 26, 573–578.

Herring, T.A., R.W. King, R.W., McClusky, S.C (2010) GPS Analysis at MIT, GAMIT Reference Manual, Release 10.5. (Department of Earth, Atmospheric, and Planetary Sciences Massachusetts Institute of Technology, Cambridge MA, available on line at http://wwwgpsg.mit.edu/~simon/gtgk/GAMIT_Ref.pdf accessed 12 May 2015).

Heublein M, Alshawaf F, Erdn Ba, Zhu X, Hinz S (2019) Compressive sensing reconstruction of 3D wet refractivity based on GNSS and InSAR observations, Journal of Geodesy, 93-2, pp 197-217.

Hirahara K (2000) Local GPS tropospheric tomography, Earth Planet. Space, 52, 935–939.

Hopfield H S (1969) Two-quartic Tropospheric Refractivity Profile for Correcting Satellite Data. Journal of Geophysical Research, 74, 4487–4499.

Ibrahim H E, El-Rabbany A (2011) Performance analysis of NOAA tropospheric signal delay model.Meas. Sci. Technol, 22, 115107.

Jolivet, R., Agram, P.S., Lin, N.Y., Simons, M., Doin, M.P., Peltzer, G., Li, Z., 2014. Improving InSAR geodesy using global atmospheric models. J. Geophys. Res. Solid Earth 119, 2324–2341. https://doi.org/10.1002/2013JB010588.

Li X, Zhang X, Ge M (2011) Regional reference network augmented precise point positioning for instantaneous ambiguity resolution. J. Geodesy 85, 151–158.

Lou Y, Huang J, Zhang W, Liang H, Zheng F, Liu J (2017) A New Zenith Tropospheric Delay Grid Product for Real-Time PPP Applications over China. Sensors, 18, 65.

Lu C, Zus F, Ge M, Heinkelmann R, Dick G, Wickert J, Schuh H (2016) Tropospheric delay parameters from numerical weather models for multi-GNSS precise positioning. Atmos. Meas. Tech. 9, 5965–5973 [CrossRef].

Lyard F, Lefevre F, Letellier T, Francis O, Modelling the global ocean tides: modern insights from FES2004 Ocean Dyn, 56 (2006), pp. 394-415, 10.1007/s10236-006-0086-x

Ma H, Verhagen S (2020) Precise Point Positioning on the Reliable Detection of Tropospheric Model Errors. Sensors, 20, 1634.

Mautz R, Ping J, Heki K, Schaffrin B, Shum C.K, Potts L (2005) Efficient spatial and temporal representations of global ionosphere maps over Japan using B-spline wavelets. Journal of Geodesy.78,660–667.

Möller, G. and Landskron, D.: Atmospheric bending effects in GNSS tomography, Atmos. Meas. Tech., 12, 23-34, https://doi.org/10.5194/amt-12-23-2019, 2019.

Perler, D., Geiger, A., & Hurter, F (2011) 4D GPS water vapor tomography: new parameterized approaches. Journal of Geodesy, 85(8), 539-550.

Ray, R. D. and Ponte R. M. Barometric tides from ECMWF operational analyses. Annales Geophysicae, 21(8):1897–1910, 2003. doi: 10.5194/angeo-21-1897-2003.

Rohm W, Bosy J (2009) Local tomography troposphere model over mountains area, Atmos. Res., 93, 777–783.

Rohm W, Zhang K, Bosy J (2014) Limited constraint, robust Kalman filtering for GNSS troposphere tomography. Atmos Meas Tech, 6, 1475-1486.

Saastamoinen J (1973) Contributions to the theory of atmospheric refraction. Part II: refraction corrections in satellite geodesy. Bull. Geod. 107:13–34.

Sadikin R, Swardiana I and Wirahman T (2017). Cubic spline interpolation for large regular 3D grid in cylindrical coordinate: (Invited paper)," 2017 International Conference on Computer, Control, Informatics and its Applications (IC3INA), Jakarta, Indonesia, 2017, pp. 1-6, doi: 10.1109/IC3INA.2017.8251730.

Shi J, Xu C, Guo J, Gao Y (2014) Local troposphere augmentation for real-time precise point positioning. Earth Planets Space, 66, 30.

Wilgan K, Hadas T, Hordyniec P, Bosy J (2017) Real-time precise point positioning augmented with high-resolution numerical weather prediction model. GPS Solut.

Yao Y, Yu C, Hu, Y (2014) A New Method to Accelerate PPP Convergence Time by using a Global Zenith Troposphere Delay Estimate Model. J. Navig, 67, 899–910. [CrossRef].

Yao Y, Zhao Q (2016) Maximally Using GPS Observation for Water Vapor Tomography. IEEE T Geosci Remote, 54, 7185-7196.

Yu W, Chen B, Dai W. Luo, X (2018) Real-Time Precise Point Positioning Using Tomographic Wet Refractivity Fields. Remote Sens. 10, 928.

Zhao Q, Yao Y, Yao W, Xia, P (2018) An optimal tropospheric tomography approach with the support of an auxiliary area, Ann. Geophys., 36, 1037–1046, https://doi.org/10.5194/angeo- 36-1037-2018.

Zumberge J F, Heflin M B, Jefferson D C, Watkins M M, Webb F H (1997) Precise point positioning for the efficient and robust analysis of GPS data from large networks. J. Geophys. Res. 12, 5005–5017. [CrossRef].

https ://unavc o.org